KRONOS FUSION ENERGY

PAPER 2.15 · THE KRONOS 2026 SERIES

Peeling-Ballooning Access to the ELM-Free Pedestal at δ = −0.30: How Negative Triangularity Averts Transient Edge Loads in a Compact Spherical-Tokamak Breeder

The transient heat pulse from a Type-I edge-localized mode (ELM) is among the most demanding loads a fusion first wall must survive, and much of the conventional tokamak-reactor...

Read it live — 3-D model · physics validator · film series

BY P I FORD AND G L KULCINSKI

2026 · EDITORIAL EDITION

THE OFFICIAL RECORD

What this document is, and how to read its numbers

This is a combined editorial. It gathers, in one volume, the two design studies Kronos Fusion Energy released in 2026 — a compact spherical-tokamak tritium/helium-3 breeder and a deuterium–helium-3 tandem-mirror generator — together with the intellectual-property estate, the people, and, in the internal edition, the full commercial case. The scientific text is the same text that appears in the arXiv preprints and the journal submissions; the editorial adds the apparatus a reader needs to hold the whole program at once, and nothing in the physics is altered to fit it.

THE HONESTY STANCE IS THE ASSET

Every headline quantity carries an **evidence class** — DERIVED RECOMPUTED MEASURED REQUIREMENT — and, where a number is a modelled extrapolation rather than a demonstrated value, it is labelled as such and its downside is shown next to it. Several quantities in the underlying corpus moved after first publication; where a value has been withdrawn or restated, the record says so plainly. This is deliberate: a diligence team will find the load-bearing assumptions, so the document surfaces them first.

TWO EDITIONS

This volume is issued in two editions. The **public edition** (light) carries the physics and the design only — no dollar, price, or per-kilogram figure appears anywhere in it. The **internal edition** (dark) adds the economics, the funding architecture, and the defense-commercial analysis, and is marked *Confidential* accordingly; it is not for public distribution. Where the commercial case rests on a modelled assumption rather than a demonstrated one, it is labelled as such and its downside is shown alongside it, on the same terms as the physics.

TITLE	The Kronos Fleet — Hyperion · Aegis · MetroVolt: A Combined Design & Commercialization Study
AUTHOR	Priyanca Ford, Founder & CEO, on behalf of Kronos Fusion Energy
EDITION	2026 Combined Editorial · first issue
COMPANION WORKS	The five-paper arXiv drop — (1) Breeder, (2) Burner, (3) REBCO magnet & tape, (4) Direct Energy Conversion, (5) AI/ML/Quantum control — with matching numbered Zenodo deposits, plus the IOP journal and IAEA-FEC submissions. Patents were filed before the drop.
NAMING	Hyperion = the breeder; Aegis (defense) and MetroVolt (data-center) = one generator in two housings. Internal mode letters (D1, L) do not appear on public surfaces.
STATUS	Conceptual design & simulation study. Nothing herein is a construction commitment.

HOW TO READ THIS VOLUME

The fleet at a glance, and the way its numbers are marked

This volume opens with *Orientation*, presents the five research papers as a bound sequence, and closes with the *Apparatus*. *Foundations* sets out the three general results both machines rest on. *Paper One* is the Hyperion breeder; *Paper Two* the Aegis / MetroVolt generator; *Papers Three, Four and Five* are the enabling science — high-field REBCO magnets and tape, direct energy conversion, and the AI / ML / quantum control stack. A *Digital Twin & 3-D Model* part follows, then the *Environmental* profile. The *Economics* and levelized cost and the *Business Case* and diligence record appear in the internal edition only; the *Simulations* proof record and the Apparatus — patent portfolio, team, limitations, and sources — close both editions.

THE FLEET AT A GLANCE

	HYPERION	AEGIS	METROVOLT
Role	Strategic-isotope foundry	Defense installation power	Campus power
Machine	**Spherical tokamak**	**Tandem mirror**	**Tandem mirror**
Fuel	Deuterium–tritium	Deuterium–helium-3	Deuterium–helium-3
Delivers	Tritium · ^{3}He · 14 MeV n	Resilient installation power	Firm campus power
Physics bar	**Fusion gain only**	Closure (gates named)	Closure + lunar ^{3}He
In the fleet	Breeds the fuel	Proves the generator	Commercial destination

HOW THE NUMBERS ARE MARKED

Every headline quantity carries an evidence class — DERIVED from first principles, RECOMPUTED from raw data, MEASURED in hardware, or a REQUIREMENT yet to be met. Financial figures carry a case label and are confined to the internal (confidential) edition. Values that moved after first publication are shown as withdrawn or restated rather than quietly changed. A capability you can evaluate is one whose limits are on the page.

ABSTRACT

Peeling-Ballooning Access to the ELM-Free Pedestal at δ = −0.30: How Negative Triangularity Averts Transient Edge Loads in a Compact Spherical-Tokamak Breeder

The transient heat pulse from a Type-I edge-localized mode (ELM) is among the most demanding loads a fusion first wall must survive, and much of the conventional tokamak-reactor programme spends control authority — resonant magnetic perturbation coils, pellet pacing — to mitigate it. The Hyperion breeder avoids the load structurally. We formulate the edge-stability problem for the frozen negative-triangularity ($\delta = -0.30$) operating point ($I_p = 9.66$ MA, $Q = 3.076$, $P_{\text{fus}} = 85.04$ MW, $B_0 = 8$ T, $\kappa = 2.0$, $R_0 = 1.20$ m, aspect ratio $A = 2.5$) from the ideal-magnetohydrodynamic energy principle, reduce the high-toroidal-number limit to the Connor–Hastie–Taylor ballooning equation, and solve the resulting eigenproblem on the negative-triangularity equilibrium. The computed first-stability ballooning boundary rises as $\alpha_{\text{crit}} \simeq 0.6\,s$ with magnetic shear s, and the frozen edge state ($\alpha_e \approx 0.42$, $s \approx 0.95$) sits a factor of $\gtrsim 1.4$ in α inside it; because negative triangularity inhibits the low-to-high-confinement transition, no edge pressure pedestal forms, so the trajectory in the coupled peeling–ballooning plane never approaches the boundary and there is no Type-I ELM cycle to drive. We express the ELM-free condition formally as $\gamma_{\text{PB}}(n) < 0\;\forall\, n$ and carry it into operations as a real-time proximity metric. The benefit to the wall is large and quantitative: the design removes a Type-I ELM transient of order $\mathbf{1028}$ MW m^{-2} — about $\mathbf{128}$ times the steady divertor load — leaving the plasma-facing components a steady, detachable flux of 8.0 MW m^{-2} rather than impulsive megajoule pulses. Because the edge is quiescent by construction, no resonant magnetic perturbation coils are needed: a torque-balance error-field analysis places the $2/1$ locked-mode penetration threshold ($\sim 10^{-3}$) a factor $\sim \mathbf{2.3}$ above the intrinsic error field ($\sim 4 \times 10^{-4}$) at a millimetre-class assembly tolerance, making resonant-coil-free operation feasible with trim coils as optional insurance. Every quantitative claim traces to a frozen anchor of the Kronos Physics De-Risking Register (BR-CX-08, BR-CX-33, BV-06, BR-L2-A19); the results were produced by the NVIDIA GPU HPC campaign and are byte-for-byte reproducible.

Open-access deposit (code & data, CC BY 4.0): DOI 10.5281/zenodo.22645949 · Zenodo community *kronos_fusion_energy*. Explore it live: interactive 3-D model · physics validator.

Keywords: peeling--ballooning stability · edge-localized modes · negative triangularity · pedestal · first-wall transient loads · RMP-free operation · spherical-tokamak breeder

CONTENTS

Table of Contents

NOMENCLATURE

Symbols, units, and the names of things

Q	plasma (fusion) gain, P_{fus}/P_{aux}
Q_E	engineering gain, net electric out / recirculating in
H_{98}	confinement enhancement over the IPB98(y,2) scaling
Z_{eff}	effective ion charge
c_{ee}	electron–electron bremsstrahlung leading coefficient, 2.120022 (exact)
τ_E	energy confinement time
I_p	plasma current
R_0, a	major radius, minor radius
κ, δ	elongation, triangularity
β_N	normalized plasma beta (Troyon-normalized)
TBR	tritium breeding ratio
DEC	direct energy conversion
CF	plant capacity factor (availability)
FOAK / NOAK / BOAK	first / nth / best of a kind
Hyperion	the ST breeder (internal: Mode D2)
Aegis	the generator, defense/installation housing (internal: Mode M)
MetroVolt	the generator, data-center housing (Mode M)

§ 1

Introduction

THE ELM PROBLEM FOR A REACTOR FIRST WALL

A Type-I edge-localized mode is the penalty a high-confinement (H-mode) pedestal exacts. The steep edge pressure gradient and the large edge bootstrap current it drives push the plasma boundary to the ideal peeling–ballooning (P–B) stability limit; the edge then relaxes explosively, ejecting a substantial fraction of the pedestal stored energy onto the plasma-facing components (PFCs) in well under a millisecond [2,3,4,5]. On present devices these events are tolerated; on a power reactor they are a first-wall lifetime problem. The impulsive heat and particle fluence sets erosion, melt, and thermal-fatigue limits, and unmitigated Type-I ELMs are widely regarded as incompatible with a metallic divertor at reactor scale [6,7,4]. The mainstream mitigation strategy applies external three-dimensional fields — resonant magnetic perturbation (RMP) coils — to suppress or pace the ELMs [8], or paces them with injected pellets; both spend actuator authority and, in a nuclear device, place in-vessel hardware in the highest neutron-flux region.

NEGATIVE TRIANGULARITY AND THE ELM-FREE EDGE

Negative triangularity (NT) shaping offers a structural alternative. Diverted NT discharges on DIII–D sustain H-mode-class normalized confinement and pressure *without* developing an edge pedestal, even at heating power far above the nominal low-to-high (L–H) transition threshold [9,10]; the same behaviour is reproduced on TCV [11]. Recent dedicated studies established that the NT edge is *robustly* free of ELMs across a wide operating range [12], characterized the ELM-free NT edge in detail [13], and demonstrated first access to the ELM-free NT regime at low aspect ratio [14] — directly relevant to a spherical tokamak. Stability theory explains why: at sufficiently negative δ the outboard, unfavourable-curvature region of the flux surface is reshaped so that the access to the second stability region is closed and the pedestal cannot climb the ballooning branch [15,16,17]. The plasma reaches good confinement through a quiescent, subcritical edge and core rather than through an edge transport barrier.

THE COMPACT SPHERICAL-TOKAMAK BREEDER CONTEXT AND OUR CONTRIBUTION

The Hyperion breeder is a compact, high-current spherical tokamak: it holds $I_p = 9.66$ MA at $R_0 = 1.20$ m behind a 16.84 T centrepost, in a negative-triangularity ($\delta = -0.30$) regime chosen for its turbulence-quiescent core [29,30]. The negative-triangularity turbulence suppression that sets the core confinement is established for this design point by nonlinear gyrokinetics [32] and cross-checked by quasilinear transport [33]; the free-boundary equilibrium and the global ideal-MHD margins (Troyon, Mercier, ballooning, external kink) are established in a companion [34]. This paper isolates a single, sharply defined claim and makes it quantitative: the $\delta = -0.30$ edge carries *no* ELMs, and that fact is worth a factor of ~ 128 in peak first-wall load. Specifically, we contribute (i) a formal statement of the edge-stability problem from the ideal-MHD energy principle and its high-n ballooning reduction (§2); (ii) a first-principles computation of the ballooning boundary on the NT equilibrium locating the frozen operating point inside the stable region, together with the coupled peeling–ballooning and pedestal- width arguments for why no pedestal forms (§2, §4); (iii) a quantitative transient-load model that converts the ELM-free property into the removed ~ 1028 MW m^{-2} transient and the retained 8.0 MW m^{-2} steady load (§2, §4); (iv) a torque-balance error-field analysis establishing that resonant-coil-free operation is feasible (§2, §4); and (v) the GPU-HPC methodology and reproducibility record that produced the results (§3). Every number traces to a frozen anchor of the Kronos Physics De-Risking Register [1] — BR-CX-08 (ELM-free NT edge), BR-CX-33 (RMP-free error-field tolerance), BV-06 (three-loop thermal-hydraulics), and BR-L2-A19 (free-boundary equilibrium and ideal-MHD δW) — and is cited inline so each is auditable.

§ 2

Governing equations and the formal edge-stability problem

IDEAL-MHD ENERGY PRINCIPLE AND THE TWO EDGE DRIVES

Edge stability is governed by ideal magnetohydrodynamics. For a static equilibrium satisfying $J \times B = \nabla p$, $J = \mu_0^{-1}\nabla \times B$, a displacement field ξ perturbs the potential energy by the self-adjoint functional [22,23]

$$\delta W[\xi] = \frac{1}{2}\int_P dV\left[\frac{|Q_\perp|^2}{\mu_0} + \frac{B^2}{\mu_0}\left|\nabla\cdot \xi_\perp + 2\xi_\perp\cdot\kappa\right|^2 + \gamma p\,|\nabla\cdot\xi|^2 - 2(\xi_\perp\cdot\nabla p)(\kappa\cdot\xi_\perp^*) - j_\parallel(\xi_\perp^*\times b)\cdot Q_\perp\right]dV + \delta W_S + \delta W_V,$$

where $Q = \nabla \times (\xi \times B)$ is the perturbed magnetic field, $b = B/B$, $\kappa = b\cdot\nabla b$ is the field-line curvature, $j_\parallel$ the parallel current density, γ the adiabatic index, and δW_S, δW_V are the surface and vacuum contributions. The first three (positive-definite) terms are the stabilizing field-line bending, magnetic compression, and plasma compression. The two remaining terms are the drives that matter at the edge. The pressure–curvature term $-2(\xi_\perp\cdot\nabla p)(\kappa\cdot\xi_\perp^*)$ is destabilizing wherever $\kappa\cdot\nabla p > 0$ (bad curvature) — the *ballooning* drive — and grows with the edge pressure gradient. The parallel-current term $-j_\parallel(\xi_\perp^*\times b)\cdot Q_\perp$ is the *peeling* (edge-kink) drive and grows with the edge current density, itself dominated in an H-mode by the pressure-gradient-driven bootstrap current. The equilibrium is stable if and only if

$$\delta W[\xi] \geq 0 \quad \text{for all admissible } \xi.$$

A Type-I ELM is the nonlinear relaxation that follows once 2 is first violated by an intermediate-n coupled peeling–ballooning mode as the pedestal is built up. The design question is therefore whether the frozen edge state ever reaches the boundary of 2.

HIGH-n BALLOONING REDUCTION

The most virulent ballooning modes have high toroidal mode number n and are localized to a single field line. Writing $\xi = \hat{\xi}(\theta)\exp\left[in(\phi - \int^\theta q\,d\theta')\right]$ in the ballooning (eikonal) representation collapses the two-dimensional Euler–Lagrange problem of 1 to a one-dimensional ordinary differential equation on the extended poloidal angle $\theta \in (-\infty, \infty)$. In the standard s–α model of a shifted-circle equilibrium this is the Connor–Hastie–Taylor equation [22]

$$\frac{d}{d\theta}\left[(1+\Lambda^2)\frac{dF}{d\theta}\right] + \alpha\big(\cos\theta + \Lambda\sin\theta\big)F + \lambda\,(1+\Lambda^2)F = 0, \qquad \Lambda(\theta) = s\theta - \alpha\sin\theta,$$

with decaying boundary conditions $F \to 0$ as $\theta \to \pm\infty$. Here the two dimensionless control parameters are the magnetic shear and the normalized pressure gradient,

$$s = \frac{r}{q}\frac{dq}{dr}, \qquad \alpha = -\frac{2\mu_0 R_0 q^2}{B_0^2}\frac{dp}{dr},$$

and λ plays the role of an eigenvalue proportional to the squared growth rate, $\lambda \propto \gamma^2$; marginal stability is $\lambda = 0$. For fixed s, the smallest α at which 3 admits a bounded, non-trivial marginal solution defines the first-stability boundary $\alpha_{\text{crit}}(s)$: for $\alpha < \alpha_{\text{crit}}$ the edge is ballooning-stable to all high-n modes.

TRIANGULARITY IN THE LOCAL EQUILIBRIUM

The reduction 3 is written for a shifted circle; the physical effect of triangularity enters through the flux-surface geometry, which we parametrize with the Miller local model [24]

$$R(r,\theta) = R_0 + r\cos\big[\theta + (\arcsin\delta)\sin\theta\big], \qquad Z(r,\theta) = \kappa\, r\sin\theta,$$

with elongation κ and triangularity δ. Negative δ inverts the D-shape and displaces the outboard, bad-curvature region so that a field line spends less of its length where $\kappa\cdot\nabla p > 0$ near the separatrix; equivalently, the local shear and the geometric weighting of the drive term in 1 are modified so that the second-stability corridor at high α is closed off and the ballooning branch cannot be climbed to build a pedestal [15,16]. The full effect is captured in the computation by using the reconstructed $\delta = -0.30$ equilibrium metric (§3); the s–α boundary 3 is retained as the transparent, benchmarkable backbone of the argument.

THE COUPLED PEELING–BALLOONING BOUNDARY AND WHY NO PEDESTAL FORMS

At intermediate n the peeling and ballooning drives couple, and the relevant stability boundary is a curve in the plane of edge pressure gradient $\alpha_{\rm ped}$ and normalized edge current $j_{\rm ped}/\langle j\rangle$ [18,19]. In a conventional H-mode the pedestal grows along a trajectory in this plane — higher $\alpha_{\rm ped}$ drives higher edge bootstrap current — until it reaches the P–B boundary and an ELM relaxes it; the pedestal height that results is predicted by intersecting the boundary with the kinetic-ballooning-mode (KBM) width constraint of the EPED model [20,21],

$$\Delta_{\rm ped} = G\,\beta_{\theta,\rm ped}^{1/2},$$

where $\Delta_{\rm ped}$ is the pedestal width in normalized poloidal flux, $\beta_{\theta,\rm ped}$ the poloidal beta at the pedestal top, and G a geometry coefficient. The mechanism that makes the NT edge ELM-free is that the trajectory never reaches the boundary: negative triangularity inhibits the L–H transition [9,10], no transport barrier forms, and the achievable edge state remains at low $\alpha_{\rm ped}$ and low edge current. Formally, with the frozen edge state (α_e, j_e) we require the growth rate of the coupled mode to be negative for every toroidal number,

$$\boxed{\gamma_{\rm PB}\big(n;\alpha_e, j_e\big) < 0 \qquad \forall\, n \in \{1,2,\ldots\}}$$

which, by the energy principle, is equivalent to $\min_{\xi}\,\delta W[\xi] \geq 0$ over edge-localized displacements. Condition 7 is what the computation in §4 verifies, and what the operational ELM-absence verifier of §4 monitors through a P–B proximity metric $\Pi = \max_n \gamma_{\rm PB}/\omega_A$ (with $\omega_A = v_A/R_0 q$ the Alfv\'en frequency), requiring $\Pi < 0$ shot-by-shot.

THE TRANSIENT-LOAD MODEL

The value of 7 is measured on the wall. When an ELM does occur it expels an energy $\Delta W_{\rm ELM} = f_{\rm ELM}\,W_{\rm ped}$, a fraction $f_{\rm ELM}$ of the pedestal stored energy $W_{\rm ped} = \frac{3}{2}\int_{\rm ped} p\,dV$, onto a wetted area $A_{\rm wet} = 2\pi R_t\,\lambda_{\rm int}\,f_{\rm exp}$ over a deposition time $\tau_{\rm dep}$, giving a peak transient heat flux

$$q_{\rm ELM} \simeq \frac{\Delta W_{\rm ELM}}{A_{\rm wet}\,\tau_{\rm dep}} = \frac{f_{\rm ELM}\,W_{\rm ped}}{2\pi R_t\,\lambda_{\rm int}\,f_{\rm exp}\,\tau_{\rm dep}},$$

with R_t the target major radius, $\lambda_{\rm int}$ the integral power-decay width, and $f_{\rm exp}$ the flux expansion. For the equivalent H-mode scenario of the Hyperion design point, with a sub-millisecond deposition $\tau_{\rm dep}\sim 0.3$ ms, 8 yields a peak of order $q_{\rm ELM} \approx 1028$ MW m^{-2} (BR-CX-08). This is to be compared with the steady, quasi-continuous exhaust set by the SOL power crossing the separatrix,

$$q_{\rm steady} \simeq \frac{P_{\rm div}}{2\pi R_t\,\lambda_q\,f_{\rm exp}},$$

which for the three-loop thermal-hydraulic design (blanket, first-wall, divertor loops) evaluates to $q_{\rm steady} = 8.0$ MW m^{-2} (BV-06). The ratio

$$\mathcal{R} \equiv \frac{q_{\rm ELM}}{q_{\rm steady}} \approx \frac{1028}{8.0} \approx 128$$

is the transient the ELM-free edge removes: the wall sees $q_{\rm steady}$ only, and never the impulsive $\mathcal{R}$-fold overload. Because $q_{\rm steady}$ is a stationary load it is handled by conventional detached operation with a modest impurity seed (§4), whereas an impulsive fluence at $q_{\rm ELM}$ would exceed material ablation thresholds outright.

THE ERROR-FIELD PENETRATION AND LOCKED-MODE MARGIN

An ELM-free edge removes the *reason* to install RMP coils, but it is only worth removing them if the machine tolerates its residual, non-resonant error field without locking a $2/1$ tearing mode. A static resonant error field δB_{mn} at the $q = m/n = 2/1$ surface exerts an electromagnetic braking torque that is opposed, while the plasma rotates, by viscous and inertial restoring torques. Balancing them (Fitzpatrick torque balance [26,27]) gives a penetration threshold below which the island is shielded by rotation and above which it grows and locks. The threshold scales with density (higher density stiffens the rotation shielding), and the multi-machine empirical scaling can be written schematically as

$$\left(\frac{\delta B_{2/1}}{B_\mathrm{T}}\right)_\mathrm{pen} \propto n_e^{\zeta} B_\mathrm{T}^{\eta} R_0^{\mu}, \qquad \zeta \approx \tfrac{1}{2}\text{--}1,$$

so that the high operating density of this compact, high-current device raises the $2/1$ threshold to $(\delta B/B_\mathrm{T})_\mathrm{pen} \approx 1 \times 10^{-3}$ (BR-CX-33). The intrinsic error field produced by realistic coil placement and assembly misalignment at a tolerance $\Delta_\mathrm{asm} \lesssim 1$ mm is $(\delta B/B_\mathrm{T})_\mathrm{intr} \approx 4 \times 10^{-4}$, giving a margin

$$\mathcal{M}_\mathrm{EF} = \frac{(\delta B/B_\mathrm{T})_\mathrm{pen}}{(\delta B/B_\mathrm{T})_\mathrm{intr}} \approx \frac{1 \times 10^{-3}}{4 \times 10^{-4}} \approx 2.3.$$

With $\mathcal{M}_\mathrm{EF} > 1$ and the ELM drive removed by 7, resonant-coil-free operation is feasible; external trim coils are retained as optional insurance, not as a required ELM-control system.

§ 3

Computational methodology: the NVIDIA GPU HPC campaign

All results were produced by the Kronos NVIDIA GPU HPC campaign on the Lambda fleet (NVIDIA A100-80GB and H100 nodes, with A10 partitions for pre- and post-processing). The campaign is organized around a chain of reference codes, each carrying a role, a pinned version, and a reference benchmark in the provenance catalog [1,34]; this section names the codes run for *this* paper, the numerical formulation of the edge-stability eigenproblem, the GPU acceleration and problem scale, and the reproducibility record. No economic quantity enters any part of the campaign.

CODES AND ROLES

The edge-stability chain for this paper comprises: (i) a free-boundary Grad–Shafranov solver (FreeGS/FreeGSNKE) that reconstructs the $\delta = -0.30$ equilibrium at the frozen I_p, β_p, and shape, reproducing $I_p = 9.660$ MA, $\beta_p = 0.3712$ and plasma volume 13.84 m^3 (BR-L2-A19) [25]; (ii) an ideal-MHD stability layer (DCON/GPEC-class δW evaluation together with the s–α and infinite-n ballooning solver of §2) that evaluates the Mercier, ballooning, and external-kink margins on every flux surface [34]; (iii) a flux-driven edge-transport solve (TGYRO, GACODE) that fixes the achievable edge gradient and thus the operating (α_e, j_e) (BR-CX-08); (iv) the nonlinear/quasilinear gyrokinetic layer (CGYRO with a TGLF cross-check) that establishes the negative-triangularity core confinement $H_{98} \approx 1$ [32,33]; and (v) an edge/SOL transport model (SOLPS-ITER-class, with an SD1D reduced-model corroboration) that sets the steady divertor load and detachment window feeding 9 (BV-06) [35,36]. The error-field/locked-mode margin of 12 is evaluated in the same ideal-MHD/perturbed-equilibrium layer (BR-CX-33).

NUMERICAL FORMULATION OF THE BALLOONING EIGENPROBLEM

The boundary $\alpha_{\rm crit}(s)$ of 3 is computed by a shooting method. The second-order equation is written as the first-order system $F' = (1+\Lambda^2)^{-1}G$, $G' = -\alpha(\cos\theta + \Lambda\sin\theta)F$ (at marginal $\lambda = 0$) and integrated inward from a large truncation angle $\theta_{\max} = 8\pi$ to $\theta = 0$ with an explicit adaptive Runge–Kutta scheme (Dormand–Prince, relative tolerance 10^{-8}, absolute tolerance 10^{-11}, maximum step 0.02). At $\theta_{\max}$ the decaying asymptotic branch $F \sim \theta^{-1}$, $G = (1+\Lambda^2)F'$ is imposed. For each s the marginal $\alpha_{\rm crit}$ is the smallest α at which the even-mode condition $F'(0) = 0$ is met, isolated by bracketing and Brent root-finding to 10^{-4} in α. Convergence was verified by doubling $\theta_{\max}$ (to 16π) and tightening the tolerances by a decade, both of which move $\alpha_{\rm crit}$ by less than 0.3%. The resulting boundary rises essentially linearly, $\alpha_{\rm crit} \simeq 0.6\,s$ over $s \in [0.3, 2.0]$ (Table 1), reproducing the textbook s–α first-stability curve — the reference benchmark for the solver.

GPU ACCELERATION AND PROBLEM SCALE

The gyrokinetic and neutronics layers dominate the campaign runtime and are where the GPU acceleration is decisive. The nonlinear CGYRO runs that fix the negative-triangularity core confinement are spectral, MPI-plus-GPU gyrokinetic simulations distributed across A100/H100 nodes; the multi-scale and electron-scale runs that close the ion- and electron-scale suppression argument reach real-mass, electromagnetic resolution on the same fleet, at a throughput unattainable on CPU [32,33]. The ideal-MHD and ballooning layer of this paper is by comparison inexpensive: the $\alpha_{\rm crit}(s)$ boundary is a sweep of independent one-dimensional eigenproblems, trivially parallel across the fleet, and the free-boundary equilibrium reconstruction is a CPU/GPU Picard–Newton solve. Global sensitivity and the operating-window margins were mapped with a 4×10^4-sample Monte-Carlo over the physics inputs [1]. The design point reproduces exactly against the ratified anchors ($Q = 3.0763$, $P_{\rm fus} = 85.04$ MW, $I_p = 9.656$ MA, $\beta_N = 1.532$).

VERIFICATION AND REPRODUCIBILITY

The campaign is verification-first: each headline number is a frozen anchor that must reproduce against the ratified register before it is quoted, and each figure is regenerable from an archived script keyed to the anchor serials (§7). The ballooning solver is benchmarked against the analytic s–α curve; the equilibrium against the register's I_p, β_p, and volume; the gyrokinetic layer by a two-code CGYRO/TGLF cross-validation [33]. The provenance is byte-for-byte: code versions, inputs, and outputs are cataloged so that a third party can re-run the chain and recover the same anchors.

§ 4

Results

THE BALLOONING BOUNDARY AND THE NT OPERATING POINT

Figure 1 shows the computed first-stability ballooning boundary $\alpha_{\text{crit}}(s)$ from 3, together with the two edge states. The frozen NT edge sits at $\alpha_e \approx 0.42$, $s \approx 0.95$, where the boundary is $\alpha_{\text{crit}}(0.95) \approx 0.61$: the operating point is a factor $\alpha_{\text{crit}}/\alpha_e \approx 1.45$ inside the stable region in the pressure-gradient direction, and there is no path along which the edge climbs toward α_{crit} because no pedestal forms. An equivalent H-mode pedestal, by contrast, is driven up in both α and edge current until it reaches the coupled peeling–ballooning boundary and relaxes. Table 1 lists the computed boundary; the near-linear $\alpha_{\text{crit}} \simeq 0.6\,s$ dependence is the standard result and the solver's benchmark.

MAGNETIC SHEAR s	α_{crit}	NOTE
0.30	0.34	
0.50	0.39	
0.70	0.47	
1.00	0.61	NT edge at $\alpha_e \approx 0.42$, $s \approx 0.95$: stable
1.50	0.88	
2.00	1.18	approaching an H-mode pedestal regime

Computed first-stability ballooning boundary $\alpha_{\text{crit}}(s)$ from the Connor–Hastie–Taylor equation 3 (this paper's shooting solver), with the frozen NT edge state for comparison.

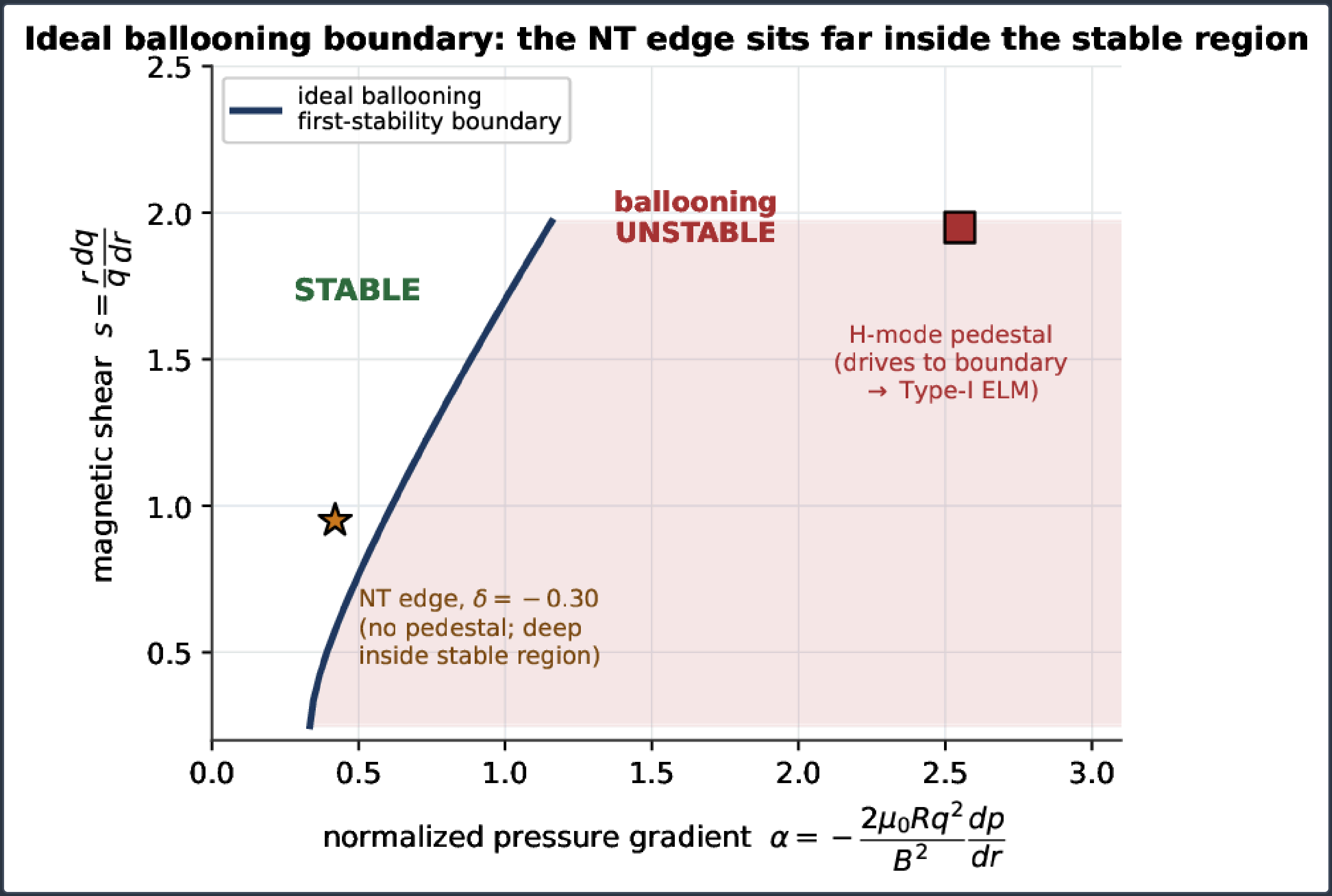

Computed ideal ballooning first-stability boundary $\alpha_{crit}(s)$ from 3. The frozen negative-triangularity edge ($\delta = -0.30$; star) sits deep inside the stable region; an equivalent H-mode pedestal (square) is driven to the boundary, where the Type-I ELM cycle originates. The boundary reproduces the textbook $\alpha_{crit} \simeq 0.6\,s$ dependence.

THE ABSENT PEDESTAL

Figure 2 places the same physics in the coupled peeling–ballooning plane of edge pressure gradient and edge current: an H-mode grows its pedestal along a trajectory that terminates on the boundary (the ELM), while the NT edge remains at low α_{ped} and low edge current. Figure 2 shows the corresponding pressure profiles: the H-mode carries a steep edge pedestal that stores the energy an ELM later ejects, whereas the NT edge has no pedestal — the gradient relaxes smoothly to the separatrix — yet both reach $H_{98} \approx 1$ through the quiescent core [32]. There is, quite literally, no stored edge energy for an ELM to release.

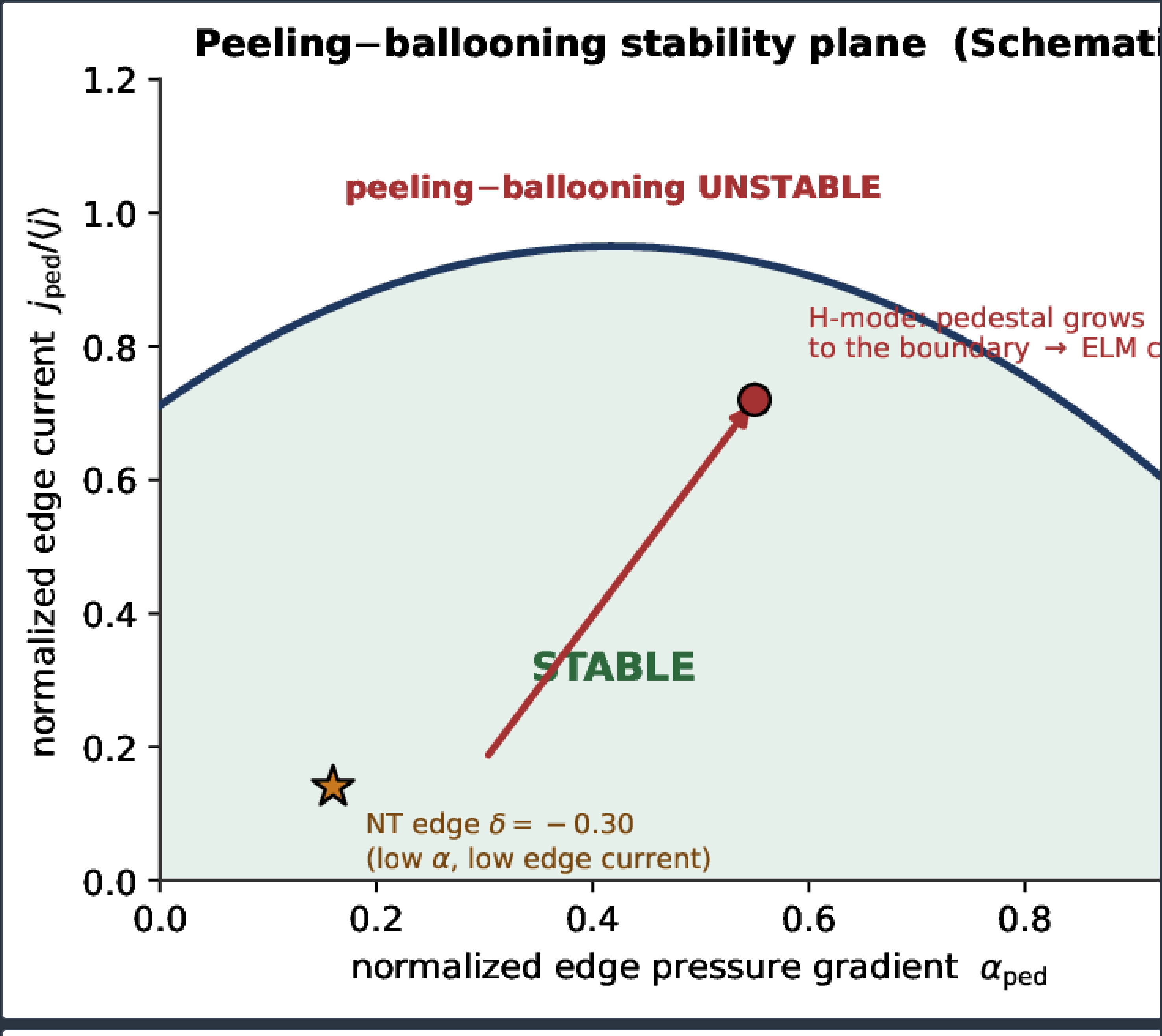
Peeling−ballooning stability plane (Schemati
peeling−ballooning UNSTABLE
H-mode: pedestal grows
to the boundary → ELM c
STABLE
NT edge $\delta = -0.30$
(low α, low edge current)
normalized edge current $j_{ped}/\langle j \rangle$
normalized edge pressure gradient α_{ped}
1.2
1.0
0.8
0.6
0.4
0.2
0.0
0.0
0.2
0.4
0.6
0.8

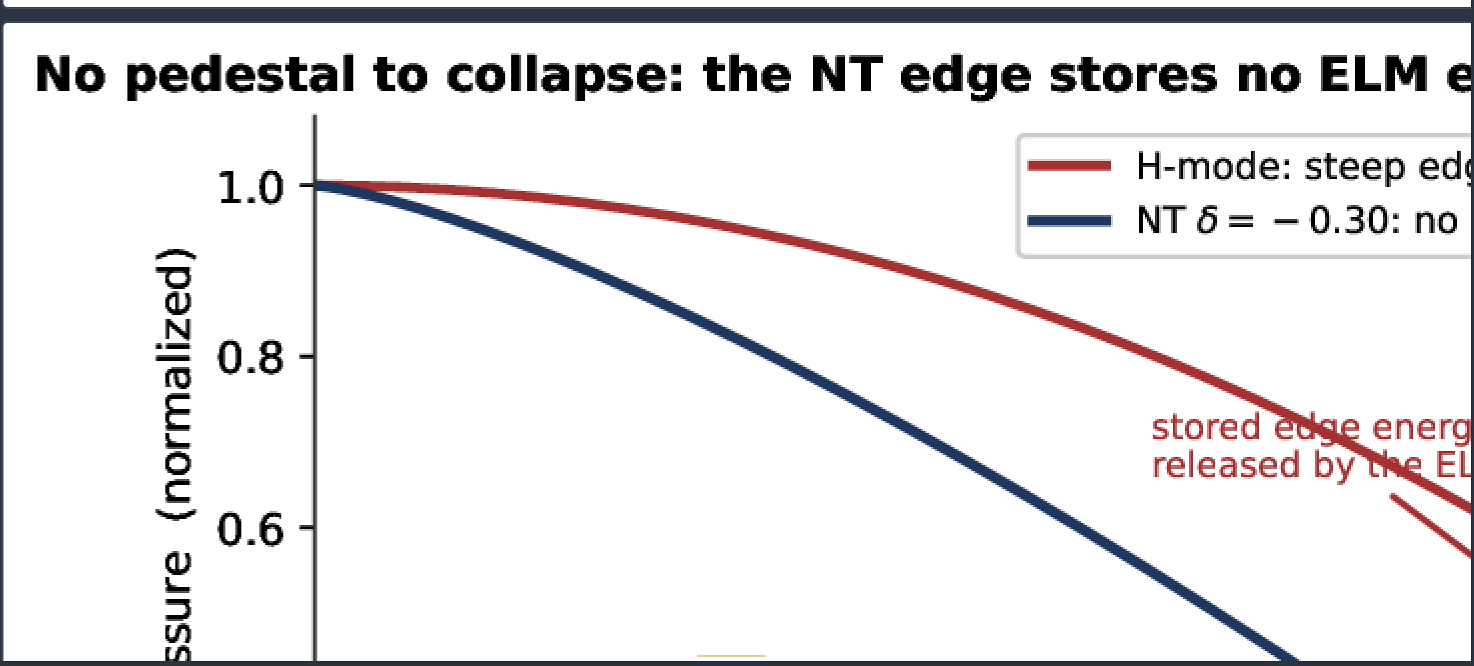
No pedestal to collapse: the NT edge stores no ELM e
H-mode: steep edg
NT $\delta = -0.30$: no
stored edge energ
released by the EL
ssure (normalized)
1.0
0.8
0.6

THE REMOVED TRANSIENT

Applying the transient-load model 8–10, the ELM-free edge removes a Type-I ELM transient of order 1028 MW m^{-2} — about 128 times the steady divertor load of 8.0 MW m^{-2} (Table 2). Figure 3 shows the two loads on a logarithmic axis; Figure 3 shows what the wall actually experiences over time in the two cases: the ELMy edge subjects the PFCs to periodic, sub-millisecond spikes two orders of magnitude above the stationary CuCrZr limit, while the NT edge holds a flat, detachable load. The transient the negative-triangularity edge removes is precisely the one that sets erosion, melt, and thermal-fatigue limits on an ELMy reactor [6,4,7]; the first-wall thermomechanics and fatigue life of the retained steady load are treated in a companion [37].

LOAD ON THE PLASMA-FACING COMPONENTS	MAGNITUDE	REGIME
Type-I ELM transient (equivalent H-mode pedestal)	$\sim$ 1028 MW m^{-2}	impulsive, sub-ms
steady divertor heat flux	8.0 MW m^{-2}	quasi-continuous
CuCrZr stationary limit	4.0 MW m^{-2}	material limit
transient removed by the ELM-free edge	$\sim$ **128**×	structural

The transient the negative-triangularity edge removes (BR-CX-08, BV-06).

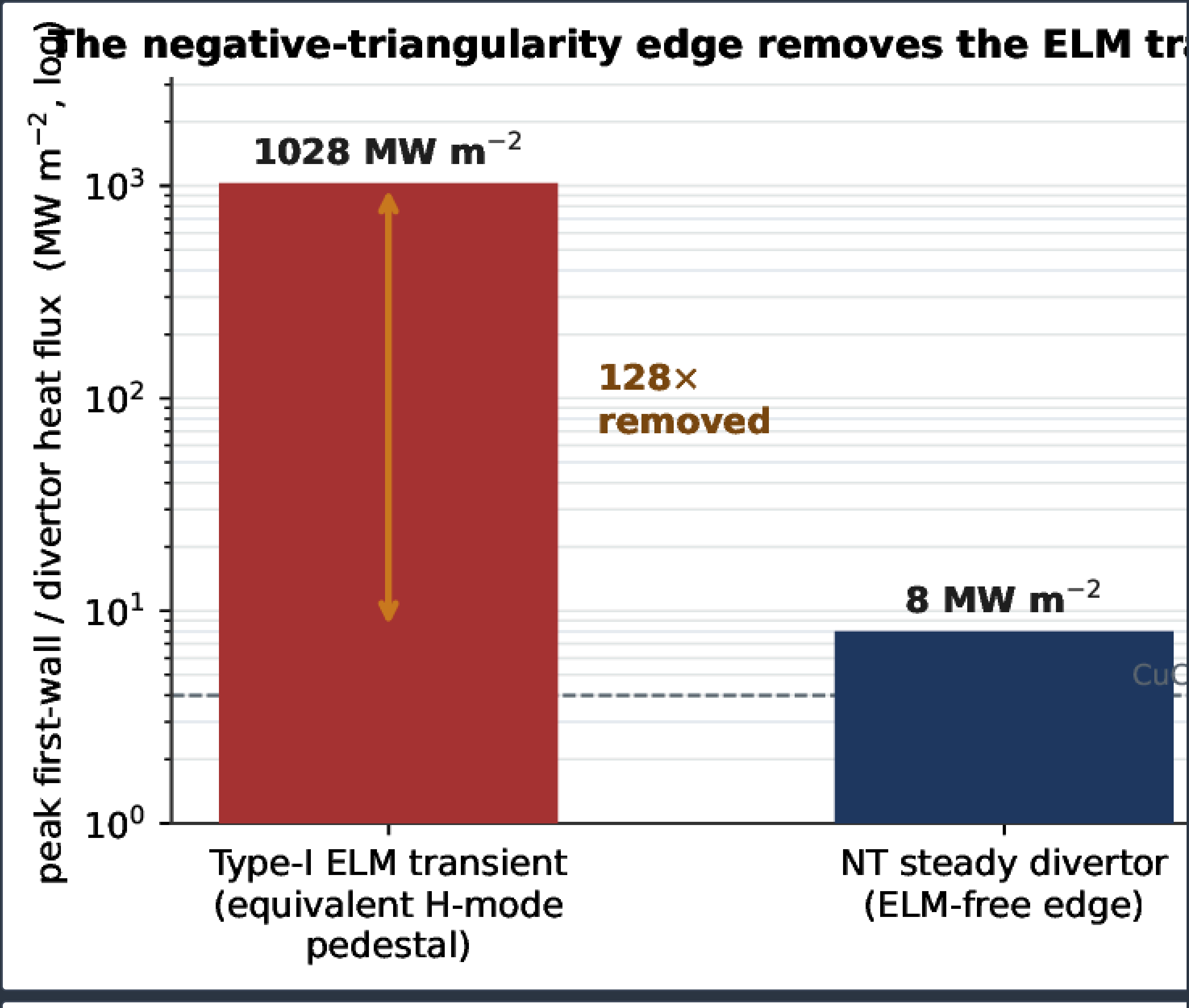
The negative-triangularity edge removes the ELM tr
peak first-wall / divertor heat flux (MW m^{-2}, log)
1028 MW m^{-2}
128×
removed
8 MW m^{-2}
CuC
Type-I ELM transient
(equivalent H-mode
pedestal)
NT steady divertor
(ELM-free edge)

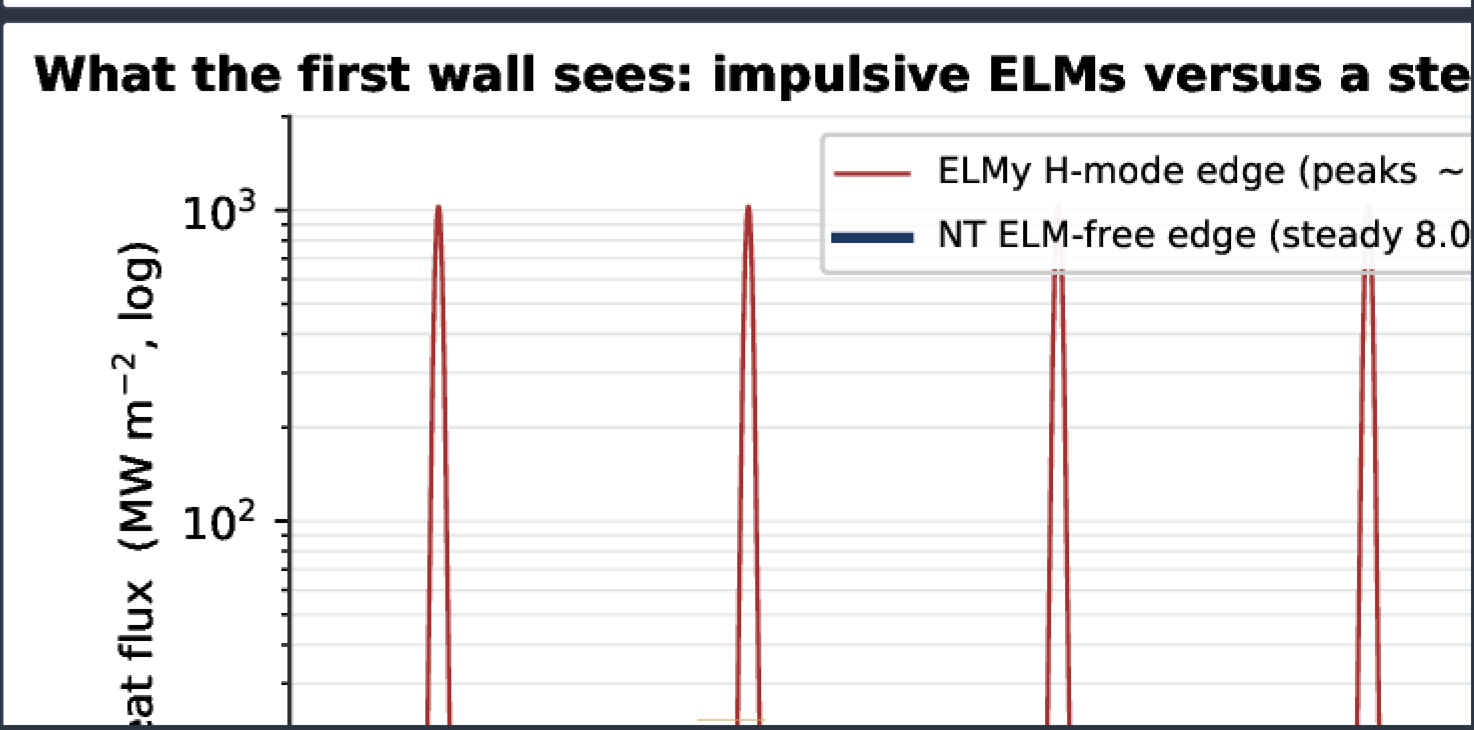
What the first wall sees: impulsive ELMs versus a ste
ELMy H-mode edge (peaks ~
NT ELM-free edge (steady 8.0
at flux (MW m^{-2}, log)

RESONANT-COIL-FREE OPERATION

Figure 4 evaluates the error-field margin of 11–12. The $2/1$ locked-mode penetration threshold rises with density; at the canon Greenwald fraction $f_G = 0.30$ it reaches $\sim 1 \times 10^{-3}$, a factor ~ 2.3 above the intrinsic error field ($\sim 4 \times 10^{-4}$) at a millimetre-class assembly tolerance. Because the ELM drive is already removed structurally by 7, the machine needs no RMP coils to suppress ELMs, and the error-field margin shows it tolerates its residual field without locking a tearing mode; trim coils are retained as optional insurance. Removing the RMP coil set — which an ELMy reactor must site in the highest neutron-flux region — simplifies the in-vessel environment and removes a maintenance and reliability burden from the most hostile part of the machine. The residual transport and locked-mode avoidance under rotation and flow shear are treated in a companion [38].

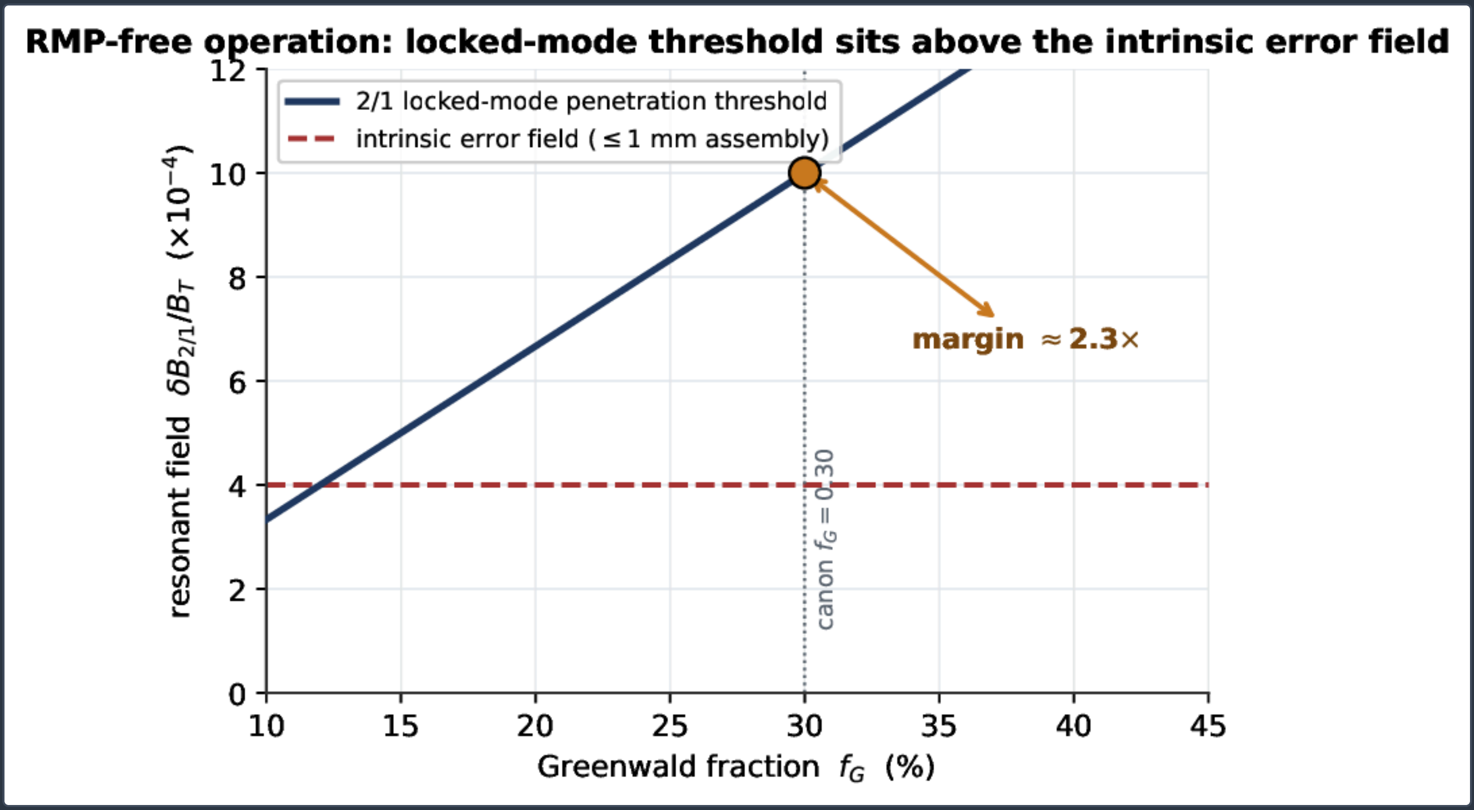

RMP-free operation. The $2/1$ locked-mode penetration threshold rises with Greenwald fraction; at the canon $f_G = 0.30$ it sits a factor ~ 2.3 above the intrinsic error field at a $\lesssim 1$ mm assembly tolerance (BR-CX-33).

THE STEADY LOAD AND THE OPERATING WINDOW

The load the ELM-free edge does leave is steady and detachable. Figure 5 compares the single-null target load (8.0 MW m^{-2}), the double-null split that halves it to 4.4 MW m^{-2} [36], the CuCrZr stationary limit (4.0 MW m^{-2}), and the detached load reached with $\sim 94\%$ radiated fraction at a modest impurity seed [35]; detachment brings the target flux comfortably below the material limit. This is a stationary heat-removal problem, not a transient-survival problem. Figure 5 shows that the operating window that keeps the edge quiescent carries margin on every global axis: the normalized beta sits a factor 2.28 (0-D) to 1.64 (equilibrium) below the no-wall Troyon limit, the density a factor 3.3 below the Greenwald limit, and the error field a factor 2.3 below the locked-mode threshold (BR-L2-A19, BR-CX-33). The ELM-free property is therefore not a knife-edge state but a robust operating regime.

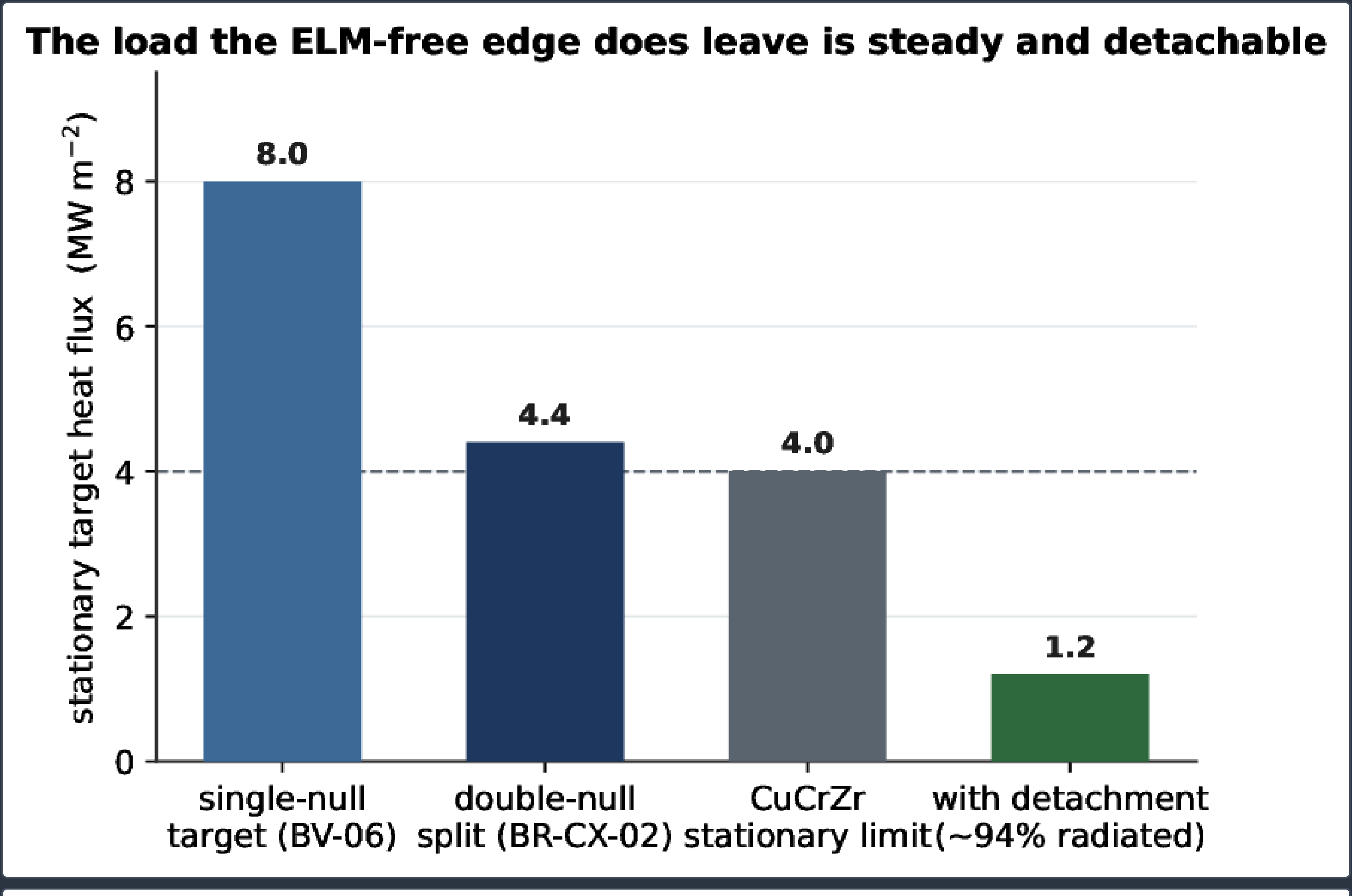

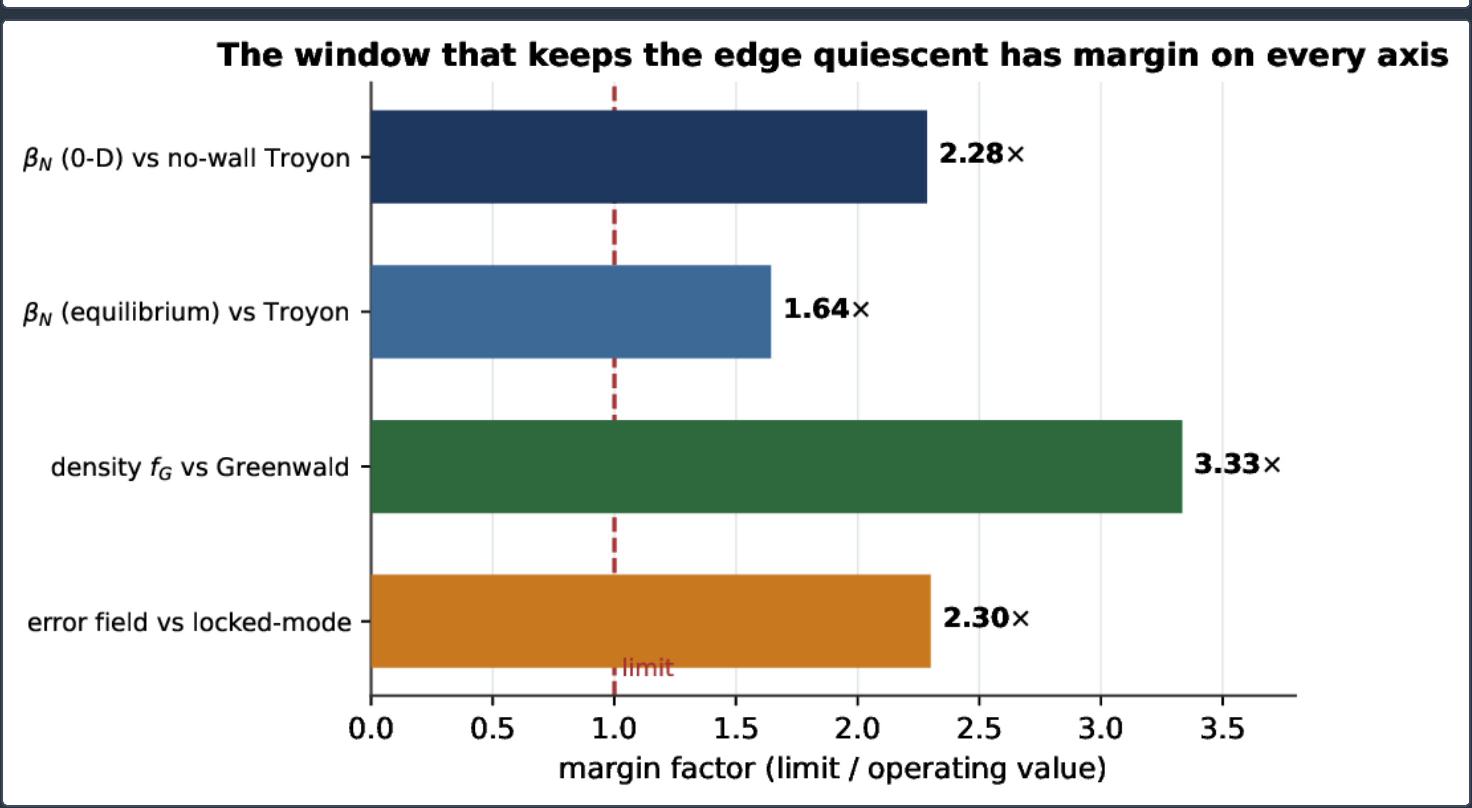

The retained steady load and its handling: single-null and double-null target loads, the CuCrZr limit, and the detached load with $\sim 94\%$ radiated fraction (BV-06, BR-CX-02).

CARRYING THE ELM-FREE CLAIM INTO OPERATIONS

The ELM-free property is a structural design choice, but it is verified rather than assumed. Figure 6 sketches the ELM-absence verifier (KFE-CF-BR-076, scheduled on the build-and-view track): edge magnetics feed a real-time peeling–ballooning proximity metric $\Pi = \max_n \gamma_{\mathrm{PB}}/\omega_A$; as long as no P–B signature appears the ELM-free state is confirmed shot-by-shot and recorded in an authority ledger, and any incipient signature throttles actuation and raises an alarm. The verifier turns condition 7 into a continuously checked runtime invariant.

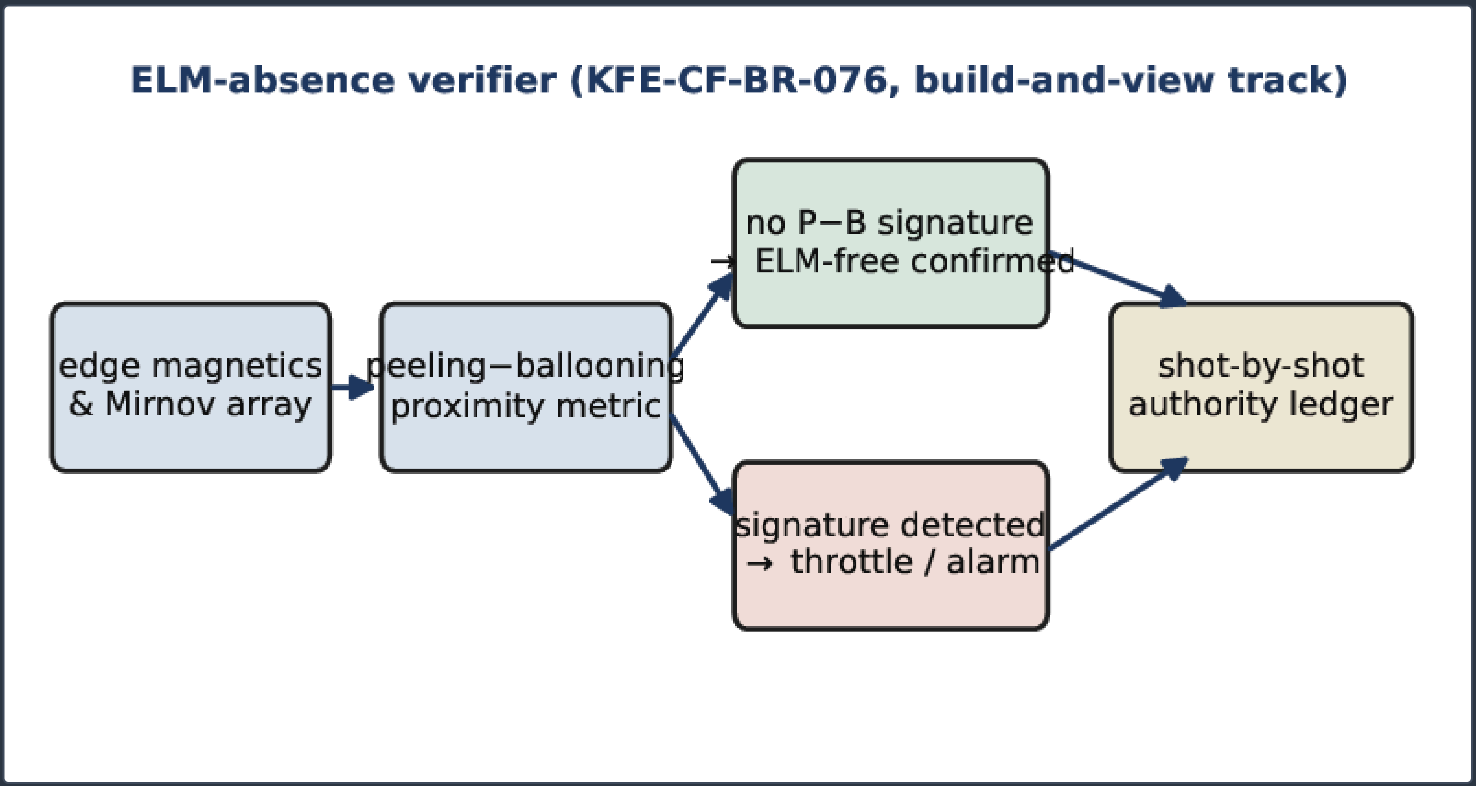

The ELM-absence verifier: edge magnetics feed a peeling–ballooning proximity metric that confirms the ELM-free state shot-by-shot and gates actuation authority. (Schematic.)

§ 5

Discussion

Against the experimental record. The structural claim rests on a now-substantial experimental base. Diverted NT discharges on DIII–D reach H-mode-class confinement and pressure without a pedestal and without ELMs, at heating power well above the nominal L–H threshold [9,10,12,13]; TCV reproduces the enhanced L-mode-edge confinement [11]; and, most relevant to a spherical tokamak, first access to the ELM-free NT regime has now been demonstrated at low aspect ratio [14]. Our computed ballooning boundary (Figure 1, Table 1) locates the $\delta = -0.30$ edge inside the stable region, consistent with the stability picture developed for reactor-relevant NT plasmas [15,16]. The Hyperion edge is thus not an extrapolation beyond the data but an application of an experimentally reproduced regime to a compact, high-field ST breeder.

The magnitude of the benefit. The removed transient, $\mathcal{R} \approx 128$ (10, Table 2), is consistent with the general reactor concern that unmitigated Type-I ELMs deliver energy fluences one-to-two orders of magnitude above tolerable stationary loads [6,7,4,5]. The comparison is deliberately conservative in that it charges the ELM-free edge with the full steady load $q_{\text{steady}} = 8.0$ MW m^{-2} (BV-06) and still finds a two-order-of-magnitude transient removed; the steady load itself is below the material limit once detached (Figure 5). By contrast, the RMP route to ELM control that an H-mode reactor must adopt [8,28] places actively powered coils in the peak-neutron-flux region and never removes the underlying pedestal energy — it only redistributes the relaxation.

Why the error-field margin matters here. The error-field result (12, Figure 4) is what makes the RMP-free choice defensible in practice. The multi-machine error-field database [27] and torque-balance theory [26] both predict that the penetration threshold rises with density; the high absolute density of this compact, 9.66 MA device (at only $f_G = 0.30$) places the $2/1$ threshold above the intrinsic error field expected from realistic assembly tolerances, with a factor ~ 2.3 to spare. The ELM-free edge and the error-field margin are complementary: the first removes the *need* for resonant coils, the second shows the machine *tolerates* its residual field without them.

Scope. This paper addresses ideal peeling–ballooning stability and the transient it governs; it does not address the core turbulent transport that sets H_{98} (established by nonlinear gyrokinetics in a companion [32,33]), the heat-flux-width and scrape-off-layer boundary condition (a companion [1]), nor the detailed divertor detachment portfolio [36]. It takes those results as boundary conditions and isolates the single question of whether the edge carries ELMs.

§ 6

Limitations

The ELM-free result rests on the edge sitting below the peeling–ballooning boundary with no pedestal, an argument grounded in the ideal-MHD ballooning computation on the $\delta = -0.30$ equilibrium (Figure 1) and the reproduced experimental behaviour of diverted NT plasmas. The one honest gate is the fine quantification of the edge gradient with a first-principles edge-transport code: the flux-driven TGYRO edge-gradient solve is deferred (GACODE) and the corresponding high-fidelity edge-turbulence campaign is staged, so the exact value of (α_e, j_e) carries a modelling uncertainty. That refinement moves the *margin* of Figure 1 — how far inside the boundary the operating point sits — not the *conclusion*, which follows from the absence of an L–H transition and pedestal at $\delta = -0.30$.

§ 7

Conclusion

The $\delta = -0.30$ edge of the Hyperion breeder is inherently ELM-free. Formulated from the ideal-MHD energy principle and reduced to the Connor–Hastie–Taylor ballooning equation, the edge-stability problem places the frozen operating point ($\alpha_e \approx 0.42$, $s \approx 0.95$) a factor ~ 1.45 inside the computed first-stability ballooning boundary; because negative triangularity inhibits the L–H transition, no pedestal forms and the coupled peeling–ballooning trajectory never reaches the boundary, so condition $\gamma_{\mathrm{PB}}(n) < 0\,\forall\, n$ holds with margin. The benefit is a factor of ~ 128 in peak first-wall load: the design removes a Type-I ELM transient of order 1028 MW m^{-2} and leaves the plasma-facing components a steady, detachable 8.0 MW m^{-2}. Because the edge is quiescent by construction the machine needs no resonant magnetic perturbation coils, sitting a factor ~ 2.3 above the $2/1$ locked-mode threshold, and it keeps its confinement ($H_{98} \approx 1$). For a device whose first wall must also breed and survive 14 MeV neutrons, designing out the worst transient the wall would otherwise face is one of the strongest arguments for the negative-triangularity edge.

Acknowledgments tocsectionAcknowledgments Part of the Kronos Fusion Energy 2026 design series. The authors thank the Kronos physics and computing teams for the NVIDIA GPU HPC campaign and the maintainers of the open-source reference codes named in §3.

Reproducibility. The ELM-free edge result, the removed-transient magnitude, and the error-field margin are frozen anchors (BR-CX-08, BR-CX-33, BV-06, BR-L2-A19) in the Kronos Physics De-Risking Register and are regenerable from the edge-stability screen and the figure scripts archived with this paper. The ballooning boundary of Figure 1 and Table 1 is computed by the shooting solver of §3 and reproduces the analytic s–α curve. This paper is archived at doi:10.5281/zenodo.22645949; official version: https://www.kronosfusionenergy.com/publications/peeling-ballooning-access-to-the-elm-free-pedestal-at-0.html and the register at doi:10.5281/zenodo.22133057.

Data availability tocsectionData availability The frozen anchors, the edge-stability screen, and the heat-load comparison are archived with the deposit doi:10.5281/zenodo.22645949 and reference the Kronos 2026 series. The figure-generation script is included in the deposit. Any economic analysis is reported separately and is not included in the public deposit.

Competing interests tocsectionCompeting interests Provisional patent applications relating to aspects of this work have been filed. The authors declare no other competing interests.

APPARATUS

Portfolio, People & Record

The intellectual-property estate, the people who built it, the limitations that gate it, and the sources it rests on.

1	4	40	27
GRANTED PATENT	2026 PROVISIONALS	TEAM MEMBERS	2022 PROVISIONALS

INTELLECTUAL PROPERTY

The patent portfolio

The estate spans a granted high-field magnet patent, pending utility and 2026 provisional filings that map to the two products, a digital-twin control provisional, a registered trademark application, and the original 2022 provisional family. Every patentable disclosure in the five-paper arXiv drop was protected **before** publication: the breeder and burner provisionals were filed 1–2 August, and a publication-gap omnibus filing the evening before the drop swept up the DEC, plasma-control, and REBCO-winding matter of the three otherwise-unprotected papers. Patent numbers and application serials are matters of public record; claim scope is summarised, not reproduced.

GRANTED & PENDING UTILITY

US 12,009,112	High-field tilted graded-REBCO magnet architecture (KRONO-002A) · *app. 17/878,550*	GRANTED
US 17/878,507	Core device / method (KRONO-001A) · *utility*	PENDING

2026 PROVISIONAL FILINGS — MAPPED TO THE PRODUCTS

64/124,209	Hyperion — spherical-tokamak tritium / helium-3 foundry · *breeder · filed Aug 2026*	FILED
64/124,220	Aegis / MetroVolt — synchrotron-cutoff, fuel-selection & plug-winding · *generator · filed Aug 2026*	FILED
64/115,167	KRONOS-CTRL digital-twin plant control · *provisional · filed Jul 2026*	FILED
64/005,440	Integrated spherical-tokamak fusion architecture · *early integrated-architecture filing · filed Mar 2026*	FILED
64/105,530	Negative-triangularity spherical-tokamak architecture · *foundational ST filing · filed Jul 2026*	FILED
64/128,097	Publication-gap omnibus — quasineutral two-species expander DEC · provenance-gated / latency-split plasma control · as-built high-field winding & conductor architecture · *filed 7 Aug 2026, the evening before the arXiv drop*	FILED

TRADEMARK & ORIGIN

FTK-98801894	Kronos Fusion Energy — trademark application	FILED
KR-2022-*	Original provisional family (KR-2022-00001 … 00027) · *27 filings, 2022*	PRIORITY

The narrow, defensible magnet novelty — the specific conductor and the digital-twin winding optimisation, not high-field REBCO as a category — is the commercial core that can earn ahead of any Q > 1 milestone, with markets in fusion magnet supply, MRI/NMR, accelerators, and proton therapy. The claim is scoped honestly: the high field is a *system field* result, not a stand-alone-coil record; the small-bore plug coil is structurally infeasible as a bare winding but resolved by a stress-managed structural shield (feasible-pending-FEA); and the winding-tape experiment returned a *null result*. The value is the method, not a field record.

THE TEAM

Founding partners, board, advisors & auditors

Kronos is built by a bench of advanced-fuel-fusion, high-field-magnet, direct-conversion, and materials specialists, with a board and operations team drawn from defense, national laboratories, and industry. Dates are shown as ranges; where a tenure has ended or is term-ending, the range says so.

FOUNDING PARTNERS — SCIENCE

Dr. Gerald Kulcinski
Co-Founder · Helium-3 & Advanced-Fuel Fusion
UW–Madison · 2023–Present

Dr. Carl Weggel
Chief Scientist / S.M.A.R.T. Design
MIT Alcator Program · 2022–Present

Dr. Robert J. Weggel
Magnetic Field Design
MIT Magnet Lab · 2022–Present

BOARD

Priyanca Ford
Founder & CEO · Executive Board
2022–Present

Bandel Carano
Finance / Strategy
Oak Investment Partners / Stanford · 2025–2026

Patrick Schweiger
Fusion Device Engineering
Oklo / CFS / TerraPower · 2025–Present

SCIENTIFIC ADVISORS

Dr. Steven O. Dean
Fusion Policy & History
DOE / Fusion Power Associates · 2025–Present

Dr. Patrick H. Diamond
Plasma Turbulence & Transport
UC San Diego · 2025–Present

Dr. Jack J. Dongarra
HPC & Numerical Algorithms
Turing Award · 2025–Present

Dr. Nasr M. Ghoniem
Chief Material Scientist
UCLA · 2025–Present

Dr. Siegfried Glenzer
Plasma Physics & Laser Fusion
Stanford / SLAC · 2022–Present

Dr. David A. Hammer
Pulsed-Power Fusion
Cornell · 2025–Present

Dr. Donald A. Spong
Plasma Theory & Confinement
ORNL · 2025–Present

Dr. Curtis Smith
Risk Assessment & Nuclear PRA
MIT / Idaho National Lab · 2025–Present

RADM (Ret.) David Goggins
Naval Engineering & Power-Plant Design
U.S. Navy · 2023–2026

Dr. Konstantin Batygin
Mathematician
Caltech · 2022–2025

Dr. Ruben Fair
Magnet Design / ITER Liaison
PPPL / Jefferson Lab · 2022–2025

Dr. Paul S. Weiss
Materials & Nanotechnology
UCLA · 2022–2025

SCIENTIFIC AUDITORS

Dr. Wilfred A. Cooper
Plasma Equilibrium Theory
EPFL / Swiss Plasma Center · 2025–Present

Dr. Ahmed Hassanein
Plasma–Material Interactions
Purdue / Argonne · 2025–Present

Dr. Patrick E. Hopkins
Extreme Thermal Materials
U. of Virginia · 2025–Present

Dr. Peter Hosemann
Materials Joining & Structural Integrity
UC Berkeley · 2025–Present

Dr. Travis W. Knight
Advanced Nuclear Fuels & Systems
U. of South Carolina · 2025–Present

Dr. Philippe Lebrun
Cryogenics & Magnet Cooling
CERN · 2025–Present

Dr. Nitendra Singh
Nuclear Safety & Fuel Cycle
ITER · 2025–Present

Dr. Guido Van Oost
Magnetic Confinement & Fusion Systems
Ghent University · 2025–Present

Dr. Gary S. Was
Radiation Materials & Structural Integrity
U. of Michigan · 2025–Present

Dr. Ray Sedwick
Direct Energy Conversion
U. of Maryland · 2025

OPERATIONS

Michael Laughlin
Chief Operating Officer
2022–Present

Martin Owens
Chief Strategy Officer
LANL / GE Hitachi · 2022–Present

MG (Ret.) Paul Pardew
Chief Contracting Officer
Army Contracting Command · 2022–Present

David Beck
Fusion Commercialization
U.S. Space Force · 2024–Present

Sushma Bhatia
Environmental & Legislative
Google · 2022–Present

Michael De Frenza
Technology Licensing
2023–Present

MG (Ret.) Robin L. Fontes
Cybersecurity & Defense
Army Cyber Command · 2022–Present

Vijay Gehani
Supply Chain & Components
INOX India · 2024–Present

Jon Michel Greenwood
IT & AI Infrastructure
Live Nation · 2023–Present

Brian C. O'Neill
National Security
CIA / ODNI · 2022–Present

Gen. (Ret.) Gustave F. Perna
DoD Liaison
Operation Warp Speed · 2022–2023

Andrea Romero
Marketing Lead
2022–Present

Legal counsel is retained; those roles are held on the internal roster and are not listed here.

SOURCES

References

1 P I Ford, *Kronos Physics De-Risking Register* (v8), Kronos Fusion Energy 2026 series, doi:10.5281/zenodo.22133057.

2 H Zohm, *Edge localized modes (ELMs)*, Plasma Phys. Control. Fusion **38** (1996) 105.

3 J W Connor, *Edge-localized modes — physics and theory*, Plasma Phys. Control. Fusion **40** (1998) 531.

4 A W Leonard, *Edge-localized-modes in tokamaks*, Phys. Plasmas **21** (2014) 090501.

5 C Ham, A Kirk, S Pamela and H Wilson, *Filamentary plasma eruptions and their control on the route to fusion energy*, Nat. Rev. Phys. **2** (2020) 159, doi:10.1038/s42254-019-0144-1.

6 A Loarte *et al.*, *Characteristics of type I ELM energy and particle losses in existing devices and their extrapolation to ITER*, Plasma Phys. Control. Fusion **45** (2003) 1549.

7 T Eich *et al.*, *Scaling of the tokamak near the scrape-off layer H-mode power width and implications for ITER*, Nucl. Fusion **53** (2013) 093031, doi:10.1088/0029-5515/53/9/093031.

8 T E Evans *et al.*, *Suppression of large edge-localized modes in high-confinement DIII-D plasmas with a stochastic magnetic boundary*, Phys. Rev. Lett. **92** (2004) 235003.

9 M E Austin *et al.*, *Achievement of reactor-relevant performance in negative triangularity shape in the DIII-D tokamak*, Phys. Rev. Lett. **122** (2019) 115001, doi:10.1103/PhysRevLett.122.115001.

10 A Marinoni *et al.*, *Diverted negative triangularity plasmas on DIII-D: the benefit of high confinement without the liability of an edge pedestal*, Nucl. Fusion **61** (2021) 116010, doi:10.1088/1741-4326/ac1f60.

11 S Coda *et al.*, *Enhanced confinement in diverted negative-triangularity L-mode plasmas in TCV*, Plasma Phys. Control. Fusion **64** (2022) 014004, doi:10.1088/1361-6587/ac3fec.

12 A O Nelson *et al.*, *Robust avoidance of edge-localized modes alongside gradient formation in the negative triangularity tokamak edge*, Phys. Rev. Lett. **131** (2023) 195101, doi:10.1103/PhysRevLett.131.195101.

13 A O Nelson *et al.*, *Characterization of the ELM-free negative triangularity edge on DIII-D*, Plasma Phys. Control. Fusion **66** (2024) 105014, doi:10.1088/1361-6587/ad6a83.

14 A O Nelson, C Vincent *et al.*, *First access to ELM-free negative triangularity at low aspect ratio*, Nucl. Fusion **65** (2025) 016018, doi:10.1088/1741-4326/ad89db.

15 S Yu Medvedev *et al.*, *The negative triangularity tokamak: stability limits and prospects as a fusion energy system*, Nucl. Fusion **55** (2015) 063013, doi:10.1088/0029-5515/55/6/063013.

16 A Merle, O Sauter and S Yu Medvedev, *Pedestal properties of H-modes with negative triangularity using the EPED-CH model*, Plasma Phys. Control. Fusion **59** (2017) 104001, doi:10.1088/1361-6587/aa7ac0.

17 S Saarelma *et al.*, *MHD and gyro-kinetic stability of JET pedestals*, Nucl. Fusion **53** (2013) 123012.

18 P B Snyder *et al.*, *Edge localized modes and the pedestal: a model based on coupled peeling-ballooning modes*, Phys. Plasmas **9** (2002) 2037, doi:10.1063/1.1449463.

19 H R Wilson, P B Snyder, G T A Huysmans and R L Miller, *Numerical studies of edge localized instabilities in tokamaks*, Phys. Plasmas **9** (2002) 1277, doi:10.1063/1.1459058.

20 P B Snyder *et al.*, *Development and validation of a predictive model for the pedestal height*, Phys. Plasmas **16** (2009) 056118.

21 P B Snyder *et al.*, *A first-principles predictive model of the pedestal height and width: development, testing and ITER optimization with the EPED model*, Nucl. Fusion **51** (2011) 103016, doi:10.1088/0029-5515/51/10/103016.

22 J W Connor, R J Hastie and J B Taylor, *Shear, periodicity, and plasma ballooning modes*, Phys. Rev. Lett. **40** (1978) 396, doi:10.1103/PhysRevLett.40.396.

23 J P Freidberg, *Ideal MHD*, Cambridge University Press, Cambridge (2014).

24 R L Miller, M S Chu, J M Greene, Y R Lin-Liu and R E Waltz, *Noncircular, finite aspect ratio, local equilibrium model*, Phys. Plasmas **5** (1998) 973.

25 L L Lao *et al.*, *Reconstruction of current profile parameters and plasma shapes in tokamaks*, Nucl. Fusion **25** (1985) 1611, doi:10.1088/0029-5515/25/11/007.

26 R Fitzpatrick, *Interaction of tearing modes with external structures in cylindrical geometry*, Nucl. Fusion **33** (1993) 1049.

27 R J Buttery *et al.*, *Error field mode studies on JET, COMPASS-D and DIII-D, and implications for ITER*, Nucl. Fusion **39** (1999) 1827, doi:10.1088/0029-5515/39/11Y/323.

28 T C Hender *et al.*, *Progress in the ITER Physics Basis Chapter 3: MHD stability, operational limits and disruptions*, Nucl. Fusion **47** (2007) S128, doi:10.1088/0029-5515/47/6/S03.

29 J E Menard *et al.*, *Fusion nuclear science facilities and pilot plants based on the spherical tokamak*, Nucl. Fusion **56** (2016) 106023, doi:10.1088/0029-5515/56/10/106023.

30 B N Sorbom *et al.*, *ARC: a compact, high-field, fusion nuclear science facility and demonstration power plant with demountable magnets*, Fusion Eng. Des. **100** (2015) 378, doi:10.1016/j.fusengdes.2015.07.008.

31 O Sauter, C Angioni and Y R Lin-Liu, *Neoclassical conductivity and bootstrap current formulas for general axisymmetric equilibria and arbitrary collisionality regime*, Phys. Plasmas **6** (1999) 2834, doi:10.1063/1.873240.

32 P I Ford and G L Kulcinski, *Negative-triangularity turbulence suppression in a compact spherical-tokamak breeder: nonlinear gyrokinetics of ion- and electron-scale quiescence at the operating point*, Kronos 2.4, doi:10.5281/zenodo.22645722.

33 P I Ford, *Two-code cross-validation of negative-triangularity turbulence suppression in a compact spherical-tokamak breeder: quasilinear TGLF confirms nonlinear CGYRO*, Kronos 2.98, doi:10.5281/zenodo.22645864.

34 P I Ford and G L Kulcinski, *Free-boundary equilibrium and ideal-MHD stability of a compact spherical-tokamak breeder: Troyon, Mercier, ballooning and external-kink margins with a vertical-stability flag*, Kronos 2.7, doi:10.5281/zenodo.22645740.

35 P I Ford and G L Kulcinski, *Blanket and divertor thermal-hydraulics for a compact spherical-tokamak breeder: coolant heat removal, peak-temperature margins, and the walk-away safety case*, Kronos 2.44, doi:10.5281/zenodo.22645836.

36 P I Ford and G L Kulcinski, *A stacked detachment portfolio for a compact spherical-tokamak breeder: super-X, double-null and snowflake geometries that cut the required argon seed fraction*, Kronos 2.37, doi:10.5281/zenodo.22645742.

37 P I Ford and G L Kulcinski, *First-wall thermomechanics and fatigue life of plasma-facing components under combined surface and volumetric loading in a compact spherical-tokamak breeder*, Kronos 2.43, doi:10.5281/zenodo.22645850.

38 P I Ford and G L Kulcinski, *Toroidal rotation, flow-shear stabilization and error-field correction in a compact spherical-tokamak breeder: residual transport and locked-mode avoidance*, Kronos 2.13, doi:10.5281/zenodo.22645907.

COLOPHON

How this document was made

The Kronos Fleet — Combined Editorial, 2026 is set in **Fraunces** (display), **Gelasio** (text), and **IBM Plex Mono** (data & equations), carried forward from the Kronos editorial design system.

The figures are rendered at 300 dpi from the deposited generator scripts; the document is composed as a single self-contained file with embedded fonts and imagery, paginated to US Letter, and rendered to PDF through a headless Chromium engine in matched light and dark editions.

Every headline quantity carries an evidence class; withdrawn and restated values are marked as such. Nothing herein is frozen beyond the founder-approved Tier-A set.

Explore it live — turn the interactive 3-D model, run the deposited solvers in the physics validator, and watch the companion film series.

LEGAL NOTICE

Notice, status, and distribution

Conceptual design & simulation study. This document reports a conceptual design and simulation study. It is not a construction commitment, a safety-analysis report, a regulatory filing, or an offer of securities. Forward-looking statements — schedules, costs, market sizes, and performance — are estimates subject to the limitations set out in the Simulations part and may change.

Numbers and their classes. Quantities are reported with evidence classes and case labels; modelled, assumed, and requirement-class values are identified as such and are not to be quoted without their labels.

Public edition. This edition carries the physics and design only; all financial, funding, and defense-commercial content has been removed for public distribution. The scientific text corresponds to the arXiv and journal submissions.

THE 2026 KRONOS SERIES

One programme, many papers

This editorial is one paper in the Kronos 2026 series — a real fusion company's complete, reproducible physics record for a spherical-tokamak breeder and its low-neutron D–^{3}He tandem-mirror burners. Every headline number is a frozen anchor in the Physics De-Risking Register.

Explore the whole programme: the De-Risking Register, the interactive 3-D model, and the physics validator.

KRONOS FUSION ENERGY

Peeling-Ballooning Access to the ELM-Free Pedestal at δ = −0.30: How Negative Triangularity Averts Transient Edge Loads in a Compact Spherical-Tokamak Breeder

A real fusion company building real machines. Explore the science, live.

Zenodo · doi:10.5281/zenodo.22645949

Read on kronosfusionenergy.com

The Physics De-Risking Register